Ceramic Proton-conducting Materials for PCFC

Jesús Gabriel Madrid-Negrín[1], Modesto González-Rodríguez[1], Stanislav Savvin[2] and Pedro Núñez[1,*].

[1] *Departamento de Química, Universidad de La Laguna, and Instituto de Materiales y Nanotecnología, PO Box 456, 38200 La Laguna, Tenerife, Spain.*

[2] Institute Laue-Langevin, 71 Avenue des martyrs, F38000, Grenoble, France

*Corresponding author: pnunez@ull.es

Abstract

This study explores the synthesis and characterization of novel proton-conducting ceramic materials based on La2-xCaxSc1-yMgyNbO7-δ, which are potential electrolytes for protonic ceramic fuel cells (PCFCs). These materials aim to combine high proton conductivity with enhanced chemical stability, suitable for intermediate temperature applications. The ceramic materials were prepared using a freeze-drying precursor method and characterized by X-ray diffraction (XRD), scanning electron microscopy (SEM), and neutron diffraction (ND). Several compositions were synthesized by co-doping with calcium and magnesium, leading to the formation of a pyrochlore structure. Electrical properties were determined using electrochemical impedance spectroscopy under different atmospheres. The results indicate that co-doping improves the relative density and enhances the conductivity, making these materials promising candidates for efficient and stable PCFC electrolytes.

1. Introduction

With the increasing concerns on the upcoming effects of the current climate crisis, renewable energies become a more than a viable response. Electrochemical devices that can convert chemical energy into electrical energy are the key for highly efficient energy conversion.[1] This type of devices includes a wide range of fuel and electrolizer cells, such as proton exchange membrane fuel cells (PEMFCs),[2–4] solid oxide fuel cells (SOFCs),[5–8] and other fuel cells.[9] Other devices that are getting more attention recently for the green hydrogen production are solid oxide electrolyser cells (SOECs).[10–14] Most of these technologies suffer from drawbacks like high cost, low chemical stability and/or low thermal stability, or highly energy demanding due to high operating temperatures. As advantages, fuel cells can convert up to 50-70% of available fuel into electricity, they have constant power production, and they allow fuel selection.[15] In terms of counteracting the disadvantages mentioned above, the Intermediate Temperature Solid Oxide Fuel Cells (IT-SOFCs) seems the most suitable devices, because it has high energy efficiency, lower operating temperature (<650ºC) and consequently, materials not so expensive.[16,17]

Proton-conducting ceramic materials are mainly used as electrolytes in ITSOFC and SOECs, also known as protonic ceramic fuel cells (PCFCs). Proton conductors exhibit higher ion conductivity at lower temperatures than usually studied electrolytes such as yttria-stabilized zirconia (YSZ),[18,19] due to a much lower activation energy needed to make

protons migrate from one electrode to another.[20] This has recently attracted the attention of the scientific world, leading to an increase in the number of published articles in this field (Figure 1).

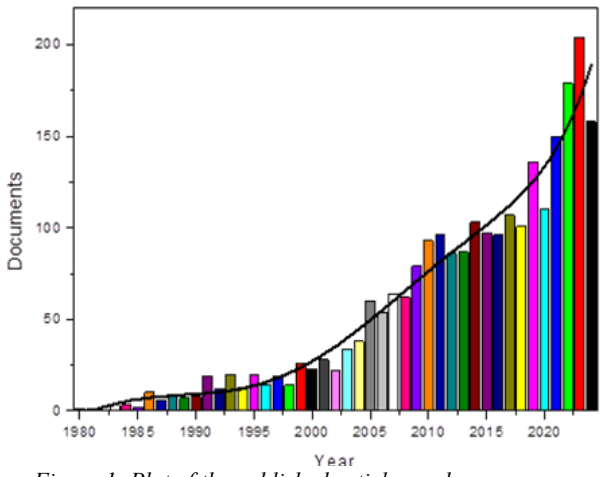

Figure 1. Plot of the published article number versus year from 1980 to present obtained from the database Scopus and using the words: proton, Conduct* and ceramic* in the section "Article title, Abstract and keywords*

The main proton conductors materials are perovskite-type based on $BaZrO_3$,[21] $BaCeO_3$[22] materials doped with rare earth elements. They show major difficulties on the processability of the materials and/or low chemical stability, which limit their potential applications.[23] Although new perovskite-type based oxides has been described exhibiting high proton conductivity and high chemical stability under oxidizing, reducing and CO_2 atmospheres. [24]

It has recently been issued that the high entropy barium cerates, i.e., $BaZr_{0.2}Sn_{0.2}Ti_{0.2}Hf_{0.2}Y_{0.2}O_{3-\delta}$[25] show good transport properties as proton conductor. The maximum power density of a PCFC was 500 mW/cm^2 at 500ºC, come together with a long-term stability, has been achieved,[26] the ensemble of the fuel cell Cathode: $PrBa_{0.5}Sr_{0.5}Co_{1.5}Fe_{0.5}O_{5+d}$ /Electrolyte: $BaZr_{0.4}Ce_{0.4}Y_{0.1}Yb_{0.1}O_{3-d}$/ Anode: $BaZr_{0.4}Ce_{0.4}Y_{0.1}Yb_{0.1}O_{3-d}$ +Ni. This PCFC operates at lower temperature, about 200ºC lower, than a conventional SOFC.[27]

The Ln_3BO_7 gives rise to a large compound family, with Ln as a trivalent lanthanide and B as a pentavalent cation, such as Nb, Ta, Sb, Ir, Mo, Ru, etc.[28] They show different space groups, being the most frequently the Cmcm,[29] but also Pnma (weberite),[30] $Fd\bar{3}m$ (pyrochlore),[31] $Fm\bar{3}m$ (deficient fluorite), [32] or $C222_1$.[28] In fact, for La_3NbO_7 it was proposed the space group Cmcm, nevertheless the structure of this phase was later refined on a single crystal prepared by flux method in the orthorhombic Pnma space group corresponding to the weberite structural type. For the lanthanide niobates, Ln_3NbO_7, it was found a weberite structural type (Pnma) for the larger lanthanides (Ln= La, Pr, Nd); a $C222_1$ space group for intermediate-size cations (Ln= Sm-Tb) and a deficient fluorite type (Fm-3m) for the smaller cations Ln^{3+} (Dy-Lu).

Proton-conducting materials, with the formula $A_2B_2O_7$, are much less studied, focusing almost all the attention on the pyrochlore lanthanum zirconate ($La_2Zr_2O_7$)[33,34] and derivatives. The strategy to improve the proton conductivity is the creation of oxygen vacancies by adding aliovalent metal as dopant with a lower oxidation state and similar ionic radius. For example, in the case of lanthanum, an ideal and commonly used dopant is Ca^{2+}, because the radii of both ions are quite close (La^{3+}, coordination 8, 130 pm; Ca^{2+}, coordination 8, 124 pm), giving rise to different dopant solubility in the phase.[35]

Pyrochlore structures are related to the fluorites. In the pyrochlore $A_2B_2O_7$ the B cations are located octahedral sites (BO_6), while A cations are in distorted cubes (AO_8), being an average coordination number of 7. It has a cubic structure, with the space group $Fd\bar{3}m$ containing eight formula

units in the unit cell (Z=8).[36] If the crystallographic origin is at the A-site, the Wyckoff sites are at *16d* (A), at *16c* (B), *48f* (O(1)) and *8a* (O(2)), having the anion vacancies at *8b*. The cation A is coordinated to eight oxygens (two O(2) and six O(1)) with a scalenohedron structure. The cation B is coordinated to six oxygens (O(1)) in a distorted octahedron, sharing corners. The O(2) anions are coordinated to four A cations, while the O(1) anions are coordinated to two A and two B cations.[37]

Proton-conducting mixed oxides have also been found in the niobate and tantalate families RE_3MO_7 (RE=La-Lu, Y; M=Nb, Ta),[38] where adding acceptor doped materials increases the oxygen vacancies and therefore, ion and proton conductivity. The substitution of one RE with a different Ln or Sc giving the structure $RE_2(B^{3+}Nb)O_7$ may give potential oxygen ion and proton conductors. This $3^+/5^+$ pyrochlore family has been even less studied than the $3^+/4^+$ ($A^{3+}{}_2B^{4+}{}_2O_7$) pyrochlores were we find the phase $La_2Zr_2O_7$. Niobates and tantalates with a 3+/5+ valence state exhibit the pyrochlore structure only when the trivalent cation at the B-site (B^{3+}) has the smallest radius. This structure is feasible when B^{3+} is either Lu or Sc.[39]

In this work, we proposed a new way of synthesizing ceramic electrolytes with pyrochlore structure using the $3^+/5^+$ pyrochlore family with the system $La_{2-x}Ca_xSc_{1-y}Mg_yNbO_{7-\delta}$ adding two different dopants in different stoichiometries. This work focuses on the following compositions: x=0.00; 0.025; 0.05; 0.075; 0.10 y=0.00;0.020;0.05; 0.10 and finally co-doping the system using the compositions that shows the best conductivity. The electrical properties as well as structure and morphology were studied.

Table 1. Cell parameters, theoretical density, experimental density, and relative density data of every material studied

Material	Cell parameter (Å)	Cell Volume ($Å^3$)	Theo. Density (g/cm^3)	Rel. Density (%)
La_2ScNbO_7	10.68	1218	5.75	92.5
$La_{1.975}Ca_{0.025}ScNbO_{6.9875}$	10.67	1215	5.73	95.8
$La_{1.95}Ca_{0.05}ScNbO_{6.975}$	10.66	1211	5.73	92.3
$La_{1.925}Ca_{0.075}ScNbO_{6.9625}$	10.66	1211	5.70	93.9
$La_{1.90}Ca_{0.10}ScNbO_{6.950}$	10.65	1208	5.68	94.5
$La_2Sc_{0.98}Mg_{0.02}NbO_{6.990}$	10.66	1211	5.78	94.8
$La_2Sc_{0.95}Mg_{0.05}NbO_{6.975}$	10.66	1211	5.77	93.9
$La_2Sc_{0.90}Mg_{0.10}NbO_{6.950}$	10.66	1211	5.75	94.8
$La_{1.90}Ca_{0.10}Sc_{0.90}Mg_{0.10}NbO_{6.900}$	10.64	1204	5.68	96.5

2. Experimental procedure

The powders were synthesized using the freeze-drying precursor method. The chemicals used in this study were La_2O_3 (Aldrich, 99,99%), Sc_2O_3 (Aldrich, 99,99%), $CaCO_3$ (Aldrich, 99,99%), MgO (Aldrich, 99,99%), citric acid (Scharlau, 99,55%), EDTA (Aldrich, 99,99%), NamOx ($(NH_4NbO(C_2O_4)_2 \cdot 6H_2O$, H.C. Starck GmbH). Previously to use La_2O_3 and Sc_2O_3 were calcinated at 900 ºC for 3h for removing humidity and CO_2. A thermogravimetric analysis was performed for NamOx to determine the percentage of Nb_2O_5

(28,63%). The lanthanum and scandium oxides were dissolved by heating in nitric acid (65%). The last one requires stronger conditions by using microwave assisted hydrothermal method. After all the cations were dissolved at low pH (<1), citric acid (CA) and diammonium EDTA salt were added to avoid the formation of metal hydroxy complexes, when the pH was increased up to 7.6 with concentrate ammonia. In a typical synthesis for 2g of final product a molar ratio of metals/CA/EDTA of 1/1/3 was used. The resulting solution was freezed by adding into liquid N_2, drop by drop, and carried to the freeze dryer (Heto LyoLab 3000). Once the sample was completely dry, the precursor became very hygroscopic and must be quickly pre-calcinated at 300ºC for 3 hours. Later it was calcinated at 800ºC for 10 hours.

The calcined powders were uniaxial pressed in form of pellets by applying two ton/cm^2. These pellets were sintered at 1500ºC for 24 hours -except for the composition x=0.10 and y=0.10 that needed 36 hours- obtaining a relative density >90%, measured by the geometric method (Table 1).

The X-ray diffraction (XRD) patterns were collected on a Panalytical XPert Pro diffractometer in the 2θ range 5º to 80º. For the Rietveld refinement parameters, it was used copper $K_{\alpha 1}$ radiation. The morphology and microstructure of the sintered materials were observed after mirror polishing and thermal etching using Scanning Electron Microscopy (SEM) on a ZEISS EVO 15 with a 2 nm resolution, coupled with a microanalyzer of X-ray dispersive energy Oxford X-MAX of 50 mm^2. The neutron scattering measurements were carried out in the D2B equipment at the Institute Laue-Langevin (ILL) in Grenoble, France. The Electrochemical Impedance Spectroscopy measurements were carried out for characterizing the electrical properties of the materials with a Frequency Response Analyzer (FRA) Solartron model 1260A, in a temperature range between 900-350ºC in six different atmospheres (dry and wet, air, argon, and argon with 5% H_2).

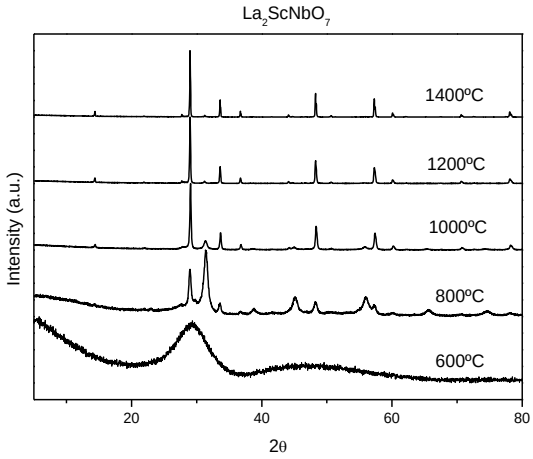

Figure 2. Evolution of the X-ray diffraction patterns of the undoped sample at different temperatures calcinated for 3 hours

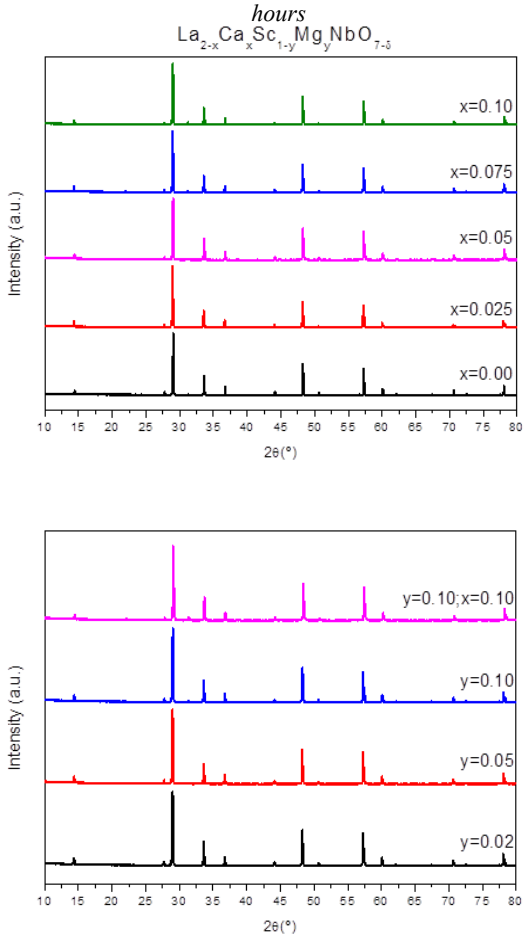

Figure 3. X-ray diffraction patterns of all samples studied in this work for the system $La_{2-x}Ca_xSc_{1-y}Mg_yNbO_{7-\delta}$ is shown. All samples were heated a 1500ºC for 24 h, except for the co-doped sample (x= 0.10 and y= 0.10).

3. Results and Discussion

3.1. Structure analysis

In Figure 2 it is shown the thermal evolution of the XRD patterns of undoped La_2ScNbO_7 samples after being calcinated at different temperatures for 3 hours. The full formation of the crystalline structure was achieved at 1400ºC. An amorphous material was observed at 600ºC; and at 800ºC a mixture of crystalline and amorphous precursors. Firstly, the crystal structure and phase compositions of the $La_{2-x}Ca_xSc_{1-y}Mg_yNbO_{7-\delta}$ series were confirmed by comparing the patterns obtained with the ICSD database structures. These ceramic materials are found to crystallize in a cubic symmetry within the space group $Fd\bar{3}m$ as reported.[39]

The powder XRD patterns of all samples sintered are shown in Figure 3. The Rietveld refinement for undoped sample is plotted in Figure 4 and Table 2 lists the most important parameters of the refinement.

The undoped and the Ca-doped sample patterns present an impurity Bragg peak at 31.2º (2θ). These secondary peaks were detected during the Rietveld refinement (Figure 4) and do not correspond to a permitted reflexion of the space group $Fd\bar{3}m$. This impurity was identified as La_3NbO_7, that means that probably in the impurity the Sc and La are partially distributed in sites *16d* (A) and *16c*, because do not detect Sc2O3 segregated. This impurity was not detected for the Mg doped samples in concentrations lower than 5 wt.%. But with a 10 wt.% of Mg, the impurity again appears as well as in the co-doping (Ca and Mg) sample. However, this impurity was not observed in the neutron diffraction (ND) patterns, due to probably that the samples for ND were prepared in another batch. Figure 5 shows the Rietveld refinement from the neutron diffraction technique of two composition of the materials obtained.

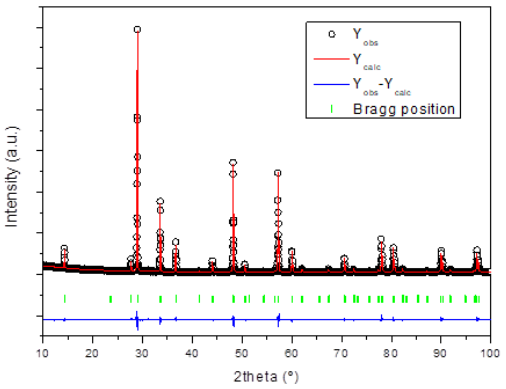

Figure 4. Rietveld Refinement of the sample $La_2ScMgNbO_7$

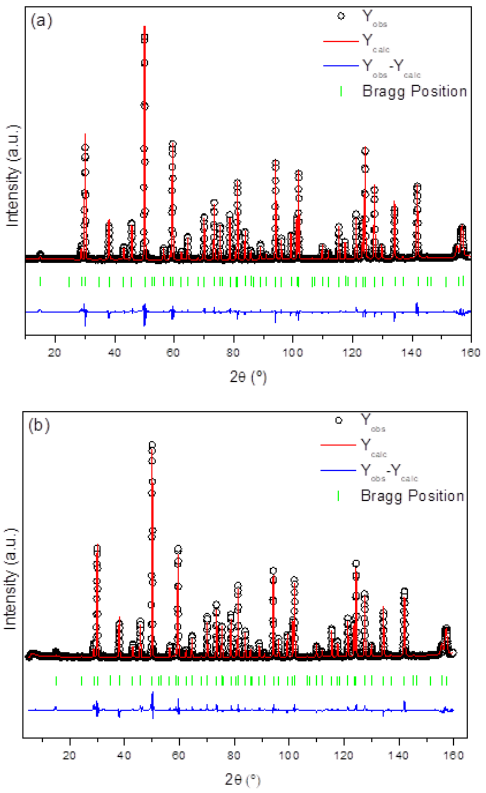

Figure 5. Rietveld Refinement of the neutron diffraction pattern for the (a) $La_2ScMgNbO_7$ sample and (b) $La_{1.95}Ca_{0.05}ScMgNbO_{6.975}$

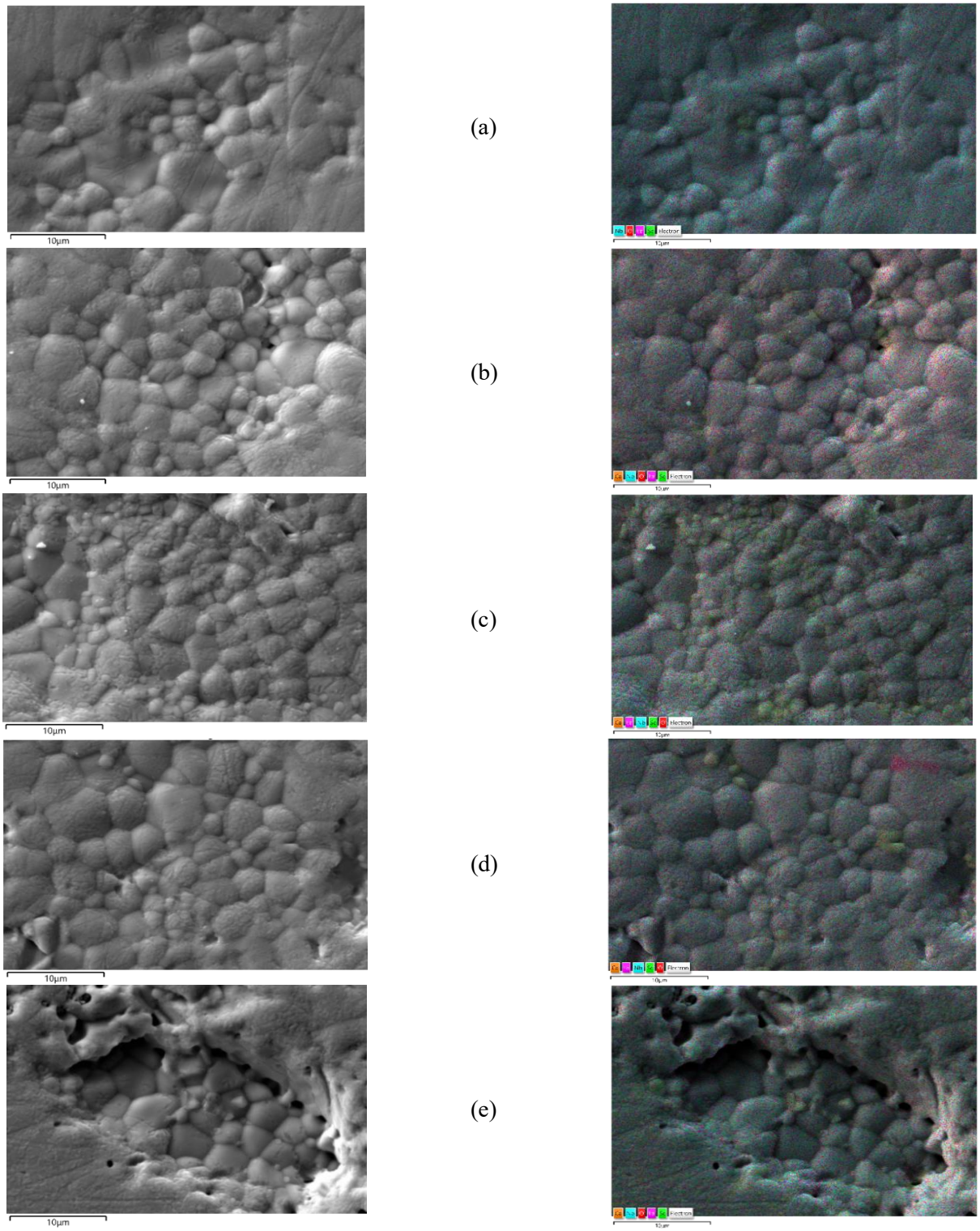

Figure 6. SEM (left) and EDX (right) images of the $La_{2-x}Ca_xMgNbO_{7-\delta}$ sintered at 1500°C for 24 hours treated with a thermal etching of 1 hour. (a) x=0.00; (b) x=0.025; (c) x=0.05; (d) x=0.075; (e) x=0.10 The colour codes are: Lanthanum (rose), Niobium (blue), Scandium (green), Calcium (orange) and oxygen (red) in the EDX images (right side).

3.2. Microstructure study

Figures 6 and 7 show the different SEM images of the undoped sample and the Ca-doped samples of the system with the respective EDX analysis used to identify the elements in the surface of the pellets. The thermal etching done first for one hour (Figure 6) and then for three hours (Figure 7) have a large difference probably due to an excessive time in the thermal etching. Both treatments show the same

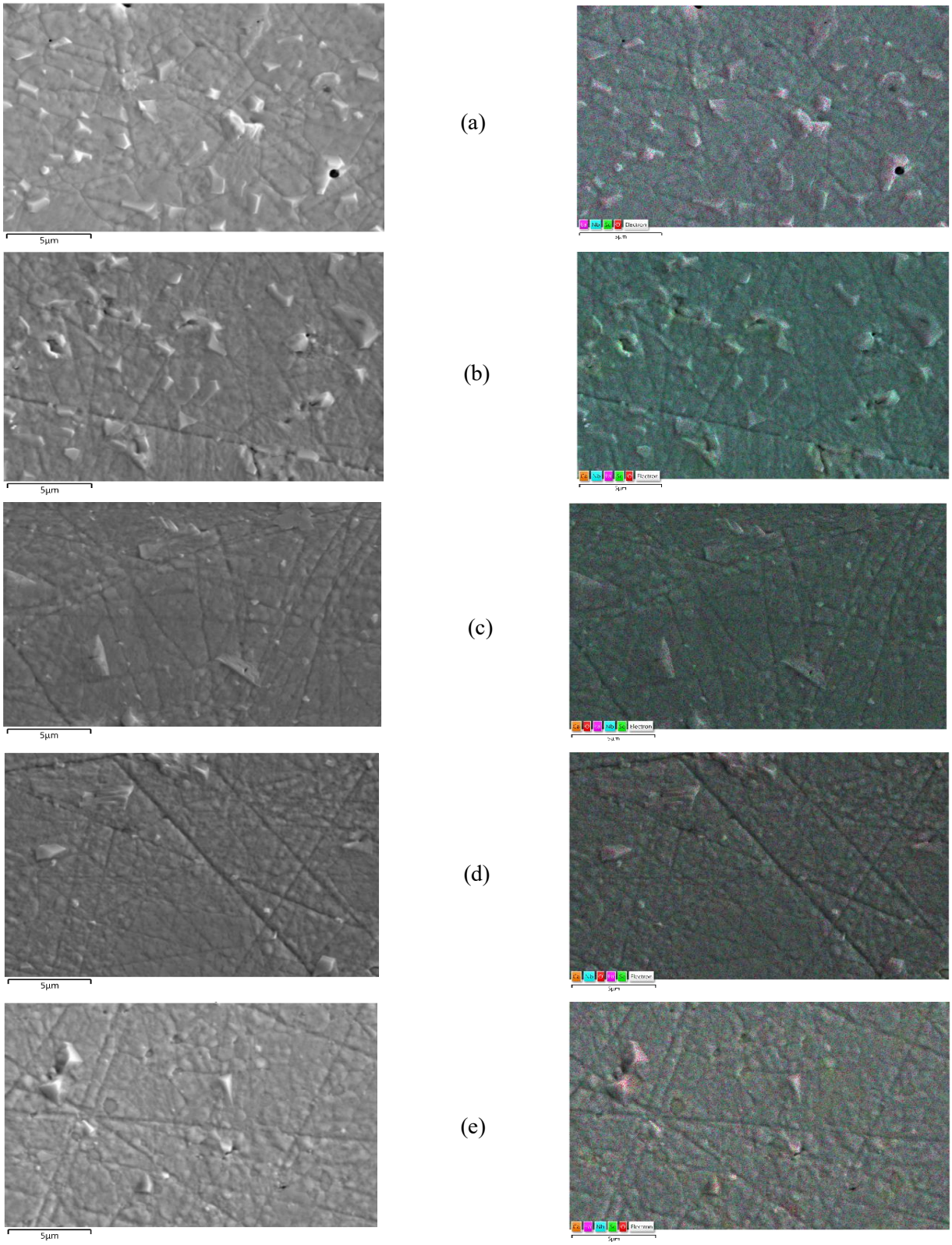

Figure 7. SEM (left) and EDX (right) images of the $La_{2-x}Ca_xMgNbO_{7-\delta}$ sintered at 1500°C for 24 hours treated with a thermal etching of 3 hours long. (a) x=0.00; (b) x=0.025; (c) x=0.05; (d) x=0.075; (e) x=0.10

distribution of elements with a homogeneous composition of the samples. In the SEM images can also be observed the successful sintering process due to the absence of holes in the surface of the materials. The average grain size does not undergo any noticeable changes with the variation of the amount of dopant.

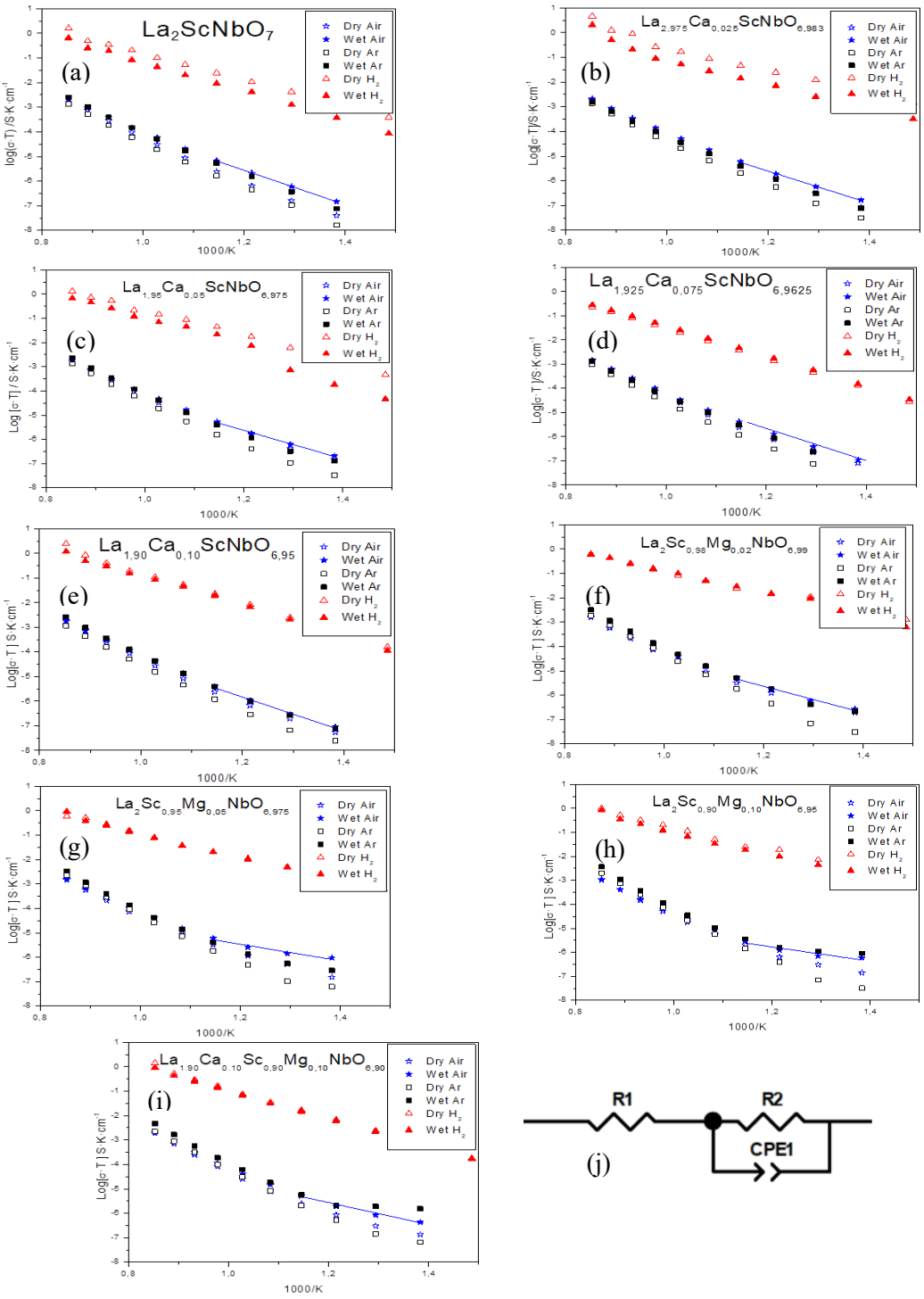

Figure 8. Arrhenius plots for the materials studied in six different atmospheres in a temperature range between 400ºC and 900ºC with the compositions: (a) La_2ScNbO_7, (b) $La_{1.975}Ca_{0.025}ScNbO_{6.9875}$, (c) $La_{1.95}Ca_{0.05}ScNbO_{6.975}$, (d) $La_{1.925}Ca_{0.075}ScNbO_{6.9625}$, (e) $La_{1.90}Ca_{0.10}ScNbO_{6.950}$, (f) $La_2Sc_{0.98}Mg_{0.02}NbO_{6.990}$, (g) $La_2Sc_{0.95}Mg_{0.05}NbO_{6.975}$, (h) $La_2Sc_{0.90}Mg_{0.10}NbO_{6.950}$, (i) $La_{1.90}Ca_{0.10}Sc_{0.90}Mg_{0.10}NbO_{6.900}$. The equivalent circuit model (j) was used to determine every resistance value obtained from the EIS measurements.

3.3. Electrical characterisation

The materials studied in this work were sintered in shape of pellets, achieving a relative density >90%. Previously to the measurements, the pellets were coated with a platinum layer and heated 950ºC for 3 hours, in order to ensure the stability of the electrode during the whole measuring process. Since the complex impedance spectra only showed a semicircle with capacitance values in the range of 10^{-}

^{8}-10^{-11} F·cm^{-1} we allocate the conductivities obtained to those of grain boundaries.[40] The values of conductivities were calculated through an equivalent circuit model that can be seen in Figure 8j, with two resistances in series. The first one (R1) correspond to a bulk resistance, because it has a significantly smaller relaxation time constant than those of grain boundary,[41] The second one (R2) correspond to the grain boundary, with a constant phase element in parallel.[42]

In wet atmospheres, the oxygen vacancies of the structure combine with water to create the proton conductivity following the next equation:

$$H_2O + O_O^X + V_O^{\bullet\bullet} \rightarrow 2(OH)_O^{\bullet},$$

The conductivity was measured in six different atmospheres (wet and dry air, argon and 5%H_2 in argon) to probe the presence of proton conductivity in our material. Figure 8 shows the Arrhenius plots of the conductivity for all samples measured in this study. The curves, at higher temperatures (left side of the Arrhenius plots) converge because the oxygen ion conductivity becomes dominant. However, at lower temperatures, the wet measures it is observed that they are more conductive than those in dry atmospheres, which confirms the presence of proton conductivity.[43] In reductive conditions, that is atmospheres that contain hydrogen, a higher conductivity is observed, probably by the appearance of n-type electronic conductivity, caused by a partial reduction of the niobium, being more conductive in hydrogen for all the samples.

Figure 9 shows the increase in the total conductivity at 500ºC in argon for the best results for the Ca-doped samples (x=0.10) and the Mg-doped samples (y=0.10), with the result of a high increase in the conductivity due to the co-doping effect (x=0.10 and y=0.10).

The activation energies calculated from the Arrhenius equation:

$$\sigma = \sigma_o \exp\left(-\frac{E_a}{kT}\right)$$

Where σ stands for the total conductivity, σ_o is the pre-exponential factor, E_a is the activation energy of the conduction process, k is the Boltzmann constant, and T is the temperature. The values of this activation energy can be seen in Table 3 for all materials prepared in this study, being better than those reported by Shlyakhtina et al. for a material with the same composition but another preparation method, having values between 1.80 eV and 1.46 eV.[39] This material able to achieve values of 0.59 eV

.

Table 2. Rietveld refinement most important parameters

La_2ScNbO_7 Volume | Å^3 = 1215---Spacial group: $Fd\bar{3}m$ #227---cubic

Atom	**Oxidation State**	**Wyckoff Position**	**X**	**Y**	**Z**	**Occ.**	**B iso**
Nb	+5.00	16 d	0.5000	0.5000	0.5000	0,5	0.563
Sc	+3.00	16 d	0.5000	0.5000	0.5000	0,5	0.463
La	+3.00	16 c	0.0000	0.0000	0.0000	1	0.563
O1	-2.00	48 f	0.4272	0.1250	0.1250	3	0.773
O2	-2.00	8 a	0.1250	0.1250	0.1250	0,5	1.098

R_p: 17.6---R_{wp}: 14.8---R_{exp}: 9.02---Chi^2:2.68

for the Mg-doped composition in wet argon at temperatures lower than 600ºC (Figure 8h) which means that there are few electronic contributions to the total conductivity, reaching values of great proton conductors with values in a range between 0.40 eV and 0.60 eV.[41,44,45] The activation energy values obtained also gives an overall view of the performance of the different amounts of dopant and type of it where the doping is beneficial for the conductivity of the materials. Although every dopant has improved the activation energy of the undoped material, the Ca-doped samples perform at lower efficiency than the Mg-doped samples, meaning that the Sc position doping can improve considerably the proton conducting properties and lower the activation energy of the conduction process.

Table 3. Activation energy values for the system of study, calculated from the measures done in wet air in <600ºC

Compound	*Wet air activation energy, eV*
La_2ScNbO_7	1.39
$La_{1.975}Ca_{0.025}ScNbO_{6.9875}$	1.29
$La_{1.95}Ca_{0.05}ScNbO_{6.975}$	1.17
$La_{1.925}Ca_{0.075}ScNbO_{6.9625}$	1.32
$La_{1.90}Ca_{0.10}ScNbO_{6.950}$	1.37
$La_2Sc_{0.98}Mg_{0.02}NbO_{6.990}$	1.08
$La_2Sc_{0.95}Mg_{0.05}NbO_{6.975}$	0.67
$La_2Sc_{0.90}Mg_{0.10}NbO_{6.950}$	0.59
$La_{1.90}Ca_{0.10}Sc_{0.90}Mg_{0.10}NbO_{6.900}$	0.76

4. Conclusions

This study successfully synthesized and characterized proton-conducting ceramic materials based on the formula $La_{2-x}Ca_xSc_{1-y}Mg_yNbO_{7-\delta}$ using a freeze-drying precursor method. The co-doping strategy with

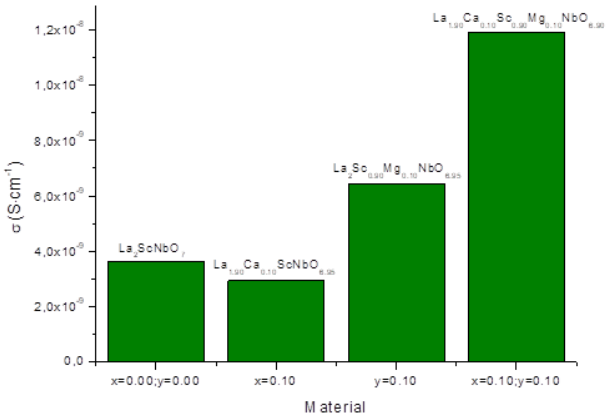

Figure 9. Different proton conductivity values for the best performing samples of each type of doping, calculated from the difference between the conductivity in dry and wet atmospheres. The measures used to calculate this data were done in argon at 500ºC

calcium and magnesium enabled the formation of a stable cubic pyrochlore structure, as confirmed by X-ray diffraction and neutron diffraction analyses. Scanning Electron Microscopy and Energy Dispersive X-ray analysis indicated a homogeneous elemental distribution and minimal porosity, affirming the successful sintering of the materials. Electrochemical impedance spectroscopy revealed that the co-doped ceramics exhibit enhanced proton conductivity compared to materials with just one dopant. The improvement in conductivity is due to increased oxygen vacancies and improved ion mobility. The materials demonstrated significant chemical stability in various atmospheric conditions. Overall, the $La_{2-x}Ca_xSc_{1-y}Mg_yNbO_{7-\delta}$ system shows great promise as an efficient and durable electrolyte for PCFC applications, highlighting its potential to advance energy conversion technologies.

CRediT authorship contribution statement

Jesús Gabriel Madrid-Negrín: Writing - original draft, Investigation, Visualization, Data curation **Modesto González-Rodríguez:** Data curation, Writing, Conceptualization. **Stanislav Savvin:** Data curation. Neutron Diffraction. **Pedro Nuñez:** Conceptualization, Supervision, Writing -Review & editing, Funding acquisition.

Declaration of competing interest

The authors declare that they have no known competing financial interests or personal relationships that could have appeared to influence the work reported in this paper.

Data availability

Data will be made available on request.

Acknowledgements

This work was supported by the project 2021 ECO-05 funded by Fundación Cajacanarias (Tenerife, Spain) and University of La Laguna.

References

(1) Jensen, S. H.; Larsen, P. H.; Mogensen, M. Hydrogen and Synthetic Fuel Production from Renewable Energy Sources. *International Journal Hydrogen Energy* **2007**, *32*(15), 3253–3257. https://doi.org/10.1016/j.ijhydene.2007.04.042.

(2) Peighambardoust, S. J.; Rowshanzamir, S.; Amjadi, M. Review of the Proton Exchange Membranes for Fuel Cell Applications. In *International Journal of Hydrogen Energy*, **2010**, 35(17), 9349–9384. https://doi.org/10.1016/j.ijhydene.2010.05.017.

(3) Carmo, M.; Fritz, D. L.; Mergel, J.; Stolten, D. A Comprehensive Review on PEM Water Electrolysis. *International Journal of Hydrogen Energy*, **2013**, 38(12), 4901–4934. https://doi.org/10.1016/j.ijhydene.2013.01.151.

(4) Borup, R.; Meyers, J.; Pivovar, B.; Kim, Y. S.; Mukundan, R.; Garland, N.; Myers, D.; Wilson, M.; Garzon, F.; Wood, D.; Zelenay, P.; More, K.; Stroh, K.; Zawodzinski, T.; Boncella, J.; McGrath, J. E.; Inaba, M.; Miyatake, K.; Hori, M.; Ota, K.; Ogumi, Z.; Miyata, S.; Nishikata, A.; Siroma, Z.; Uchimoto, Y.; Yasuda, K.; Kimijima, K. I.; Iwashita, N. Scientific Aspects of Polymer Electrolyte Fuel Cell Durability and Degradation. *Chemical Reviews*, **2007**, 107(10), 3904–3951. https://doi.org/10.1021/cr050182l.

(5) Jacobson, A. J. Materials for Solid Oxide Fuel Cells. *Chemistry of Materials*, **2010**, 22(3), 660–674. https://doi.org/10.1021/cm902640j.

(6) Shimura, K.; Nishino, H.; Kakinuma, K.; Brito, M. E.; Uchida, H. Effect of Samaria-Doped Ceria (SDC) Interlayer on the Performance of La0.6Sr0.4Co0.2Fe0.8O3-δ/SDC Composite Oxygen Electrode for Reversible Solid Oxide Fuel Cells. *Electrochimica Acta* **2017**, *225*, 114–120. https://doi.org/10.1016/j.electacta.2016.12.100.

(7) Brett, D. J. L.; Atkinson, A.; Brandon, N. P.; Skinner, S. J. Intermediate Temperature Solid Oxide Fuel Cells. *Chemical Society Reviews* **2008**, *37* (8), 1568–1578. https://doi.org/10.1039/b612060c.

(8) Steele, B. C. H. *Appraisal of Ce1−yGdyO2−y/2 electrolytes for IT-SOFC operation at 500°C*. Solid State Ionics, **2000**, 129 (1-4), 95-110. https://doi.org/10.1016/S0167-2738(99)00319-7

(9) Ferriday, T. B.; Middleton, P. H. Alkaline Fuel Cell Technology - A Review. *International Journal of Hydrogen Energy*, **2021**, 46 (35), 18489–18510. https://doi.org/10.1016/j.ijhydene.2021.02.203.

(10) Schmidt, O.; Gambhir, A.; Staffell, I.; Hawkes, A.; Nelson, J.; Few, S. Future Cost and Performance of Water Electrolysis: An Expert Elicitation Study. *International Journal of Hydrogen Energy* **2017**, *42* (52), 30470–30492. https://doi.org/10.1016/j.ijhydene.2017.10.045.

(11) Khan, M. S.; Xu, X.; Knibbe, R.; Zhu, Z. Air Electrodes and Related Degradation Mechanisms in Solid Oxide Electrolysis and Reversible Solid Oxide Cells. *Renewable and Sustainable Energy Reviews*, **2021**, 143, 110918 https://doi.org/10.1016/j.rser.2021.110918.

(12) Hauch, A.; Küngas, R.; Blennow, P.; Hansen, A. B.; Hansen, J. B.; Mathiesen, B. V.; Mogensen, M. B. Recent Advances in Solid Oxide Cell Technology for Electrolysis. *Science,* **2020**, *370* (6513). https://doi.org/10.1126/science.aba6118.

(13) Schmidt, O.; Gambhir, A.; Staffell, I.; Hawkes, A.; Nelson, J.; Few, S. Future Cost and Performance of Water Electrolysis: An Expert Elicitation Study. *International Journal of Hydrogen Energy* **2017**, *42* (52), 30470–30492. https://doi.org/10.1016/j.ijhydene.2017.10.045.

(14) Kim, S. J.; Kim, S. W.; Park, Y. M.; Kim, K. J.; Choi, G. M. Effect of Gd-Doped Ceria Interlayer on the Stability of Solid Oxide Electrolysis Cell. *Solid State Ionics* **2016**, *295*, 25–31. https://doi.org/10.1016/j.ssi.2016.07.007.

(15) Stambouli, A. B.; Traversa, E. *Fuel Cells, an Alternative to Standard Sources of Energy*. Renewable and Sustainable Energy Reviews, **2002**, 6 (3), 297-306. https://doi.org/10.1016/S1364-0321(01)00015-6

(16) Su, H.; Hu, Y. H. Progress in Low-Temperature Solid Oxide Fuel Cells with Hydrocarbon Fuels. *Chemical Engineering Journal*, **2020**, 402, 126235 https://doi.org/10.1016/j.cej.2020.126235.

(17) Singhal, S. C. *Advances in Solid Oxide Fuel Cell Technology*. Solid State Ionics, **2000**, 135, 305-313. https://doi.org/10.1016/S0167-2738(00)00452-5

(18) Scherrer, B.; Schlupp, M. V. F.; Stender, D.; Martynczuk, J.; Grolig, J. G.; Ma, H.; Kocher, P.; Lippert, T.; Prestat, M.; Gauckler, L. J. On Proton Conductivity in Porous and Dense Yttria Stabilized Zirconia at Low Temperature. *Advanced Functional Materials* **2013**, *23* (15), 1957–1964. https://doi.org/10.1002/adfm.201202020.

(19) Mahato, N.; Banerjee, A.; Gupta, A.; Omar, S.; Balani, K. Progress in Material Selection for Solid Oxide Fuel Cell Technology: A Review. *Progress in Materials Science*, **2015**,

72, 141–337. https://doi.org/10.1016/j.pmatsci.2015.01.001.

(20) Zhang, W.; Hu, Y. H. Progress in Proton-Conducting Oxides as Electrolytes for Low-Temperature Solid Oxide Fuel Cells: From Materials to Devices. *Energy Science and Engineering*, **2021**, 984–1011. https://doi.org/10.1002/ese3.886.

(21) Hyun Ryu, K.; Haile, S. M. *Chemical Stability and Proton Conductivity of Doped $BaCeO_3$-$BaZrO_3$. Solid Solutions*. Solid State Ionics, **1999**, 125, 355-367. https://doi.org/10.1016/S0167-2738(99)00196-4

(22) Taniguchi, N.; Hatoh, K.; Niikura, J.; Gamo, T.; Iwahara, H. *Proton Conductive Properties of Gadolinium-Doped Barium Cerates at High Temperatures*. Solid State Ionics **1992**, 53-56, 998-1003. https://doi.org/10.1016/0167-2738(92)90283-U

(23) Loureiro, F. J. A.; Nasani, N.; Reddy, G. S.; Munirathnam, N. R.; Fagg, D. P. A Review on Sintering Technology of Proton Conducting BaCeO3-BaZrO3 Perovskite Oxide Materials for Protonic Ceramic Fuel Cells. *Journal of Power Sources* **2019**, 438, 2266991. https://doi.org/10.1016/j.jpowsour.2019.226991.

(24) Saito, K.; Yashima, M. High Proton Conductivity within the 'Norby Gap' by Stabilizing a Perovskite with Disordered Intrinsic Oxygen Vacancies. *Nature Communications* **2023**, *14* (1). https://doi.org/10.1038/s41467-023-43122-4.

(25) Gazda, M.; Miruszewski, T.; Jaworski, D.; Mielewczyk-Gryń, A.; Skubida, W.; Wachowski, S.; Winiarz, P.; Dzierzgowski, K.; Łapiński, M.; Szpunar, I.; Dzik, E. Novel Class of Proton Conducting Materials - High Entropy Oxides. *ACS Materials Letters,* **2020**, *2* (10), 1315–1321. https://doi.org/10.1021/acsmaterialslett.0c00257.

(26) Choi, S.; Kucharczyk, C. J.; Liang, Y.; Zhang, X.; Takeuchi, I.; Ji, H. Il; Haile, S. M. Exceptional Power Density and Stability at Intermediate Temperatures in Protonic Ceramic Fuel Cells. *Nature Energy,* **2018**, *3* (3), 202–210. https://doi.org/10.1038/s41560-017-0085-9.

(27) Shim, J. H. Ceramics Breakthrough. *Nature Energy*, **2018**, *3* (3), 168–169. https://doi.org/10.1038/s41560-018-0110-7.

(28) Siqueira, K. P. F.; Soares, J. C.; Granado, E.; Bittar, E. M.; De Paula, A. M.; Moreira, R. L.; Dias, A. Synchrotron X-Ray Diffraction and Raman Spectroscopy of Ln 3NbO7 (Ln=La, Pr, Nd, Sm-Lu) Ceramics Obtained by Molten-Salt Synthesis. *Journal of Solid State Chemistry*, **2014**, *209*, 63–68. https://doi.org/10.1016/j.jssc.2013.10.015.

(29) H.J. Rossell. Fluorite-Related Phases Ln3MO7, Ln = Rare Earth, Y or Sc, M = Nb, Sb, or Ta: II. Structure Determination. *Journal of Solid State Chemistry,* **1979**, *27* (1), 115–122. https://doi.org/https://doi.org/10.1016/0022-4596(79)90150-6.

(30) A. Kahn-Harari; L. Mazerolles; D. Michel; F. Robert. Structural Description of La3NbO7. *Journal*

Solid State Chemistry **1995**, 103–106. https://doi.org/https://doi.org/10.1006/jssc.1995.1189.

(31) Fennell, T.; Bramwell, S.; Green, M. Structural and Magnetic Characterization of Ho. *Canadian Journal of Physics*, **2001**, *79*, 1415–1419. https://doi.org/10.1139/cjp-79-11/12-1415.

(32) Doi, Y.; Harada, Y.; Hinatsu, Y. Crystal Structures and Magnetic Properties of Fluorite-Related Oxides Ln3NbO7 (Ln=lanthanides). *Journal of Solid State Chemistry* **2009**, *182* (4), 709–715. https://doi.org/10.1016/j.jssc.2008.12.012.

(33) Zhao, P.; Zheng, H.; Li, G.; Geng, Y.; Xiao, Y.; Guo, H.; Peng, P. Mechanical Properties, Thermophysical Properties and Electronic Structure of Yb3+ or Ce4+-Doped La2Zr2O7-Based TBCs. *Journal of Rare Earths*. Editorial Office of Chinese Rare Earths, **2023**, 588–598. https://doi.org/10.1016/j.jre.2022.03.015.

(34) Lavanya, D.R., Darshan, G.P., Malleshappa, J. *et al.* One material, many possibilities via enrichment of luminescence in $La_2Zr_2O_7$:Tb^{3+} nanophosphors for forensic stimuli aided applications. Scientific Reports, **2022**, 12, 8898. https://doi.org/10.1038/s41598-022-11980-5

(35) Xiang, P.; Ismail, S. A.; Guo, S.; Jiang, L.; Han, D. Fluorite-Based Proton Conducting Oxides: Structures, Materials and Applications. *Materials Advances*, **2024**, 5, 12–29. https://doi.org/10.1039/D3MA00367A

(36) Chakoumakos, B. C. *Systematics of the Pyrochlore Structure Type, Ideal A2B2X6Y*; *Journal of Solid State Chemistry* **1984**, 53 (1), 120-129. https://doi.org/10.1016/0022-4596(84)90234-2

(37) Nandi, S.; Jana, Y. M.; Sarkar, S.; Jana, R.; Mukherjee, G. D.; Gupta, H. C. Synthesis, Structure, UV–Vis–NIR, Infrared and Raman Spectroscopy, and Force-Field Investigation for A2GaSbO7 (A3+ = Y, Dy, Gd) Pyrochlores. *Journal of Alloys and Compounds,* **2019**, *771*, 89–99. https://doi.org/10.1016/j.jallcom.2018.08.235.

(38) Chesnaud, A.; Braida, M. D.; Estradé, S.; Peiró, F.; Tarancón, A.; Morata, A.; Dezanneau, G. High-Temperature Anion and Proton Conduction in RE3NbO7 (RE=La, Gd, Y, Yb, Lu) Compounds. *Journal of the European Ceramic Society,* **2015**, *35*(11), 3051–3061. https://doi.org/10.1016/j.jeurceramsoc.2015.04.014.

(39) Shlyakhtina, A. V.; Pigalskiy, K. S.; Belov, D. A.; Lyskov, N. V.; Kharitonova, E. P.; Kolbanev, I. V.; Borunova, A. B.; Karyagina, O. K.; Sadovskaya, E. M.; Sadykov, V. A.; Eremeev, N. F. Proton and Oxygen Ion Conductivity in the Pyrochlore/Fluorite Family of Ln2-: XCaxScMO7-δ (Ln = La, Sm, Ho, Yb; M = Nb, Ta; X = 0, 0.05, 0.1) Niobates and Tantalates. *Dalton Transactions* **2018**, *47* (7), 2376–2392. https://doi.org/10.1039/c7dt03912c.

(40) Irvine, J.T.S., Sinclair, D.C. and West, A.R. (**1990**), Electroceramics: Characterization by Impedance Spectroscopy. Advance Materials,**1990**, 2(3), 132-138.

https://doi.org/10.1002/adma.19900020304

(41) Yu, S.; Wang, Z.; Yang, L.; Liu, J.; Guan, R.; Xiao, Y.; He, T. Enhancing the Sinterability and Electrical Properties of BaZr0.1Ce0.7Y0.2O3-δ Proton-Conducting Ceramic Electrolyte. *Journal of the American Ceramic Society* **2021**, *104* (1), 329–342. https://doi.org/10.1111/jace.17467.

(42) Lyagaeva, J. G.; Vdovin, G. K.; Medvedev, D. A. Distinguishing Bulk and Grain Boundary Transport of a Proton-Conducting Electrolyte by Combining Equivalent Circuit Scheme and Distribution of Relaxation Times Analyses. *Journal of Physical Chemistry,* **2019**, *123* (36), 21993–21997. https://doi.org/10.1021/acs.jpcc.9b05705.

(43) Liu, Y.; Guo, Y.; Ran, R.; Shao, Z. A Novel Approach for Substantially Improving the Sinterability of BaZr0.4Ce0.4Y0.2O3-δ Electrolyte for Fuel Cells by Impregnating the Green Membrane with Zinc Nitrate as a Sintering Aid. *Journal of Membrane Science,* **2013**, *437*, 189–195. https://doi.org/10.1016/j.memsci.2013.03.002.

(44) Kasyanova, A. V.; Lyagaeva, J. G.; Vdovin, G. K.; Murashkina, A. A.; Medvedev, D. A. Transport Properties of LaYbO3-Based Electrolytes Doped with Alkaline Earth Elements. *Electrochimica Acta* **2023**, *439*. https://doi.org/10.1016/j.electacta.2022.141702.

(45) Amsif, M.; Marrero-López, D.; Magrasó, A.; Peña-Martínez, J.; Ruiz-Morales, J. C.; Núñez, P. Synthesis and Characterisation of BaCeO3-Based Proton Conductors Obtained from Freeze-Dried Precursors. *Journal of the European Ceramic Society,* **2009**, *29* (1), 131–138. https://doi.org/10.1016/j.jeurceramsoc.2008.06.001.